View metadata, citation and similar papers at core.ac.uk

brought to you by CORE

provided by Archive Ouverte en Sciences de l'Information et de la Communication

Grid Voltages Estimation for Three-Phase PWM Rectifiers Control Without AC Voltage Sensors

Adel Rahoui, Ali Bechouche, Hamid Seddiki, Djafar Ould Abdeslam

To cite this version:

Adel Rahoui, Ali Bechouche, Hamid Seddiki, Djafar Ould Abdeslam. Grid Voltages Estimation for Three-Phase PWM Rectifiers Control Without AC Voltage Sensors. IEEE Transactions on Power Electronics, Institute of Electrical and Electronics Engineers, 2018, 33 (1), pp.859-875. 10.1109/TPEL.2017.2669146 . hal-02306230

HAL Id: hal-02306230

https://hal.archives-ouvertes.fr/hal-02306230

Submitted on 9 Oct 2019

HAL is a multi-disciplinary open access archive for the deposit and dissemination of scientific research documents, whether they are published or not. The documents may come from teaching and research institutions in France or abroad, or from public or private research centers.

L'archive ouverte pluridisciplinaire **HAL**, est destinée au dépôt et à la diffusion de documents scientifiques de niveau recherche, publiés ou non, émanant des établissements d'enseignement et de recherche français ou étrangers, des laboratoires publics ou privés.

Grid Voltages Estimation for Three-Phase PWM Rectifiers Control Without AC Voltage Sensors

Adel Rahoui, Ali Bechouche, Hamid Seddiki, and Djaffar Ould Abdeslam, *Senior Member, IEEE*

***Abstract*—This paper proposes a new AC voltage sensorless control scheme for three-phase pulse-width modulation rectifier. A new startup process to ensure a smooth starting of the system is also proposed. The sensorless control scheme uses an adaptive neural (AN) estimator inserted in voltage-oriented control to eliminate the grid voltage sensors. The developed AN estimator combines an adaptive neural network in series with an adaptive neural filter. The AN estimator structure leads to simple, accurate and fast grid voltages estimation, and makes it ideal for low cost digital signal processor implementation. Lyapunov based stability and parameters tuning of the AN estimator are performed. Simulation and experimental tests are carried out to verify the feasibility and effectiveness of the AN estimator. Obtained results show that; the proposed AN estimator presented faster convergence and better accuracy than the second order generalized integrator based estimator; the new startup procedure avoided the over-current and reduced the settling time; the AN estimator presented high performances even under distorted and unbalanced grid voltages.**

***Index Terms*—AC voltage sensorless control, adaptive neural (AN) estimator, grid voltages estimation, neural networks (NNs), pulse-width modulation (PWM) rectifier, startup process, voltage-oriented control (VOC).**

I. Introduction

NOWADAYS, renewable energy sources such as photovoltaic and wind power generation systems are commonly connected to the grid through three-phase pulse-width modulation (PWM) rectifier [1], [2]. This converter topology has such advantages as low harmonic pollution, adjustable DC-link voltage, bidirectional energy flow and operation at unity power factor (UPF) [3]. In renewable energy generation systems, cost reduction is essential for increasing their attractiveness compared to other conventional energy sources [1], [4]. So, decreasing the converters cost can leads to improve their competitiveness.

Usually, control scheme of the three-phase grid connected PWM rectifier consist of two control loops; one for tracking AC-line currents, and another to regulate the DC-link voltage [5]. To perform this, at least five sensors are generally required; two grid voltage sensors, one DC-link voltage sensor, and two AC-line current sensors [6]–[11]. However, operation with reduced number of sensors provides cost savings. Indeed, for mid-low power systems, the sensors cost covers a significant portion of the entire system cost [12], [13]. For high power systems, the sensors cost is less significant since the overall system cost is high. Nevertheless, even if sensors are installed, control scheme with sensorless operation ability is relevant [4], [12]. This ensures uninterrupted operation in case of sensors failure. Besides obvious benefits of sensors reduction, there are several other additional advantages like [4], [8], [11], [13], [14]; elimination of noise, resolution limitations, offset and various disturbances related to sensors, and decrease of hardware complexity. AC-line current sensors and DC-link voltage sensor are essential for proper operation of the control system since the AC-line currents and DC-link voltage are the controlled quantities [9]. In addition, these sensors are employed for overcurrent and overvoltage protections [4], [9]. On the other hand, grid voltage sensors are mainly used for synchronization purposes. So, they can be replaced by software sensors. Various strategies for grid voltages sensorless control of PWM rectifiers have been developed. Some of them are discussed in what follow.

Sensorless control algorithm based on instantaneous power theory has been initially proposed in [15]. Grid voltages are estimated by adding the input voltages to the voltage drop on the AC filter. Despite its simplicity, the AC-line currents derivative is required. Since this solution presents high noise sensitivity, other methods have been developed using virtual flux (VF) concept [9], [10], [16]–[21], Kalman filters [22], [23], disturbance observers [14], [24], hybrid parallel observers [25] and Luenberger observers [26]. Adaptive full-order observers [12], [27] have been also proposed for grid voltage sensorless control. This strategy has been tested under unbalanced conditions by exploiting the filtering capabilities of reduced-order generalized integrators (ROGIs). In [11], ROGI based control scheme has been modified to achieve sensorless operation. One cycle control designed using hardware circuits instead of a digital algorithm has been presented in [8]. Recent algorithms based on virtual impedance emulation [4] and mathematical optimization [6], [7] have been investigated. Other alternatives using neural networks (NNs) have been proposed for grid voltages estimation [28], [29]. In [28], the authors have developed a sensorless deadbeat current control strategy based on a multilayer NN estimator. Accordingly, an uncertainty function containing the AC filter parameters variation, harmonics disturbances and grid voltages information, is used for

A. Rahoui, A. Bechouche, and H. Seddiki are with the L2CSP Laboratory, Mouloud Mammeri University, BP 17 RP 15000 Tizi-Ouzou, Algeria (e-mail: adel-rahoui@live.fr; ali_bechouche@yahoo.fr; sedikihamid2004@yahoo.fr).

D. Ould Abdeslam is with the MIPS Laboratory, University of Haute Alsace, 61 rue Albert Camus, F-68093 Mulhouse, France (e-mail: djaffar.ould-abdeslam@uha.fr).

synchronization and control purposes. Separate estimation of the AC filter parameters and grid voltages using a parallel NNs structure has been achieved in [29].

Although the cited strategies provide satisfactory results, some of them require specific control schemes [8], [11], [14], [24], [28]. Others are sensitive to load variation [4], need initialization [7] and present instability under grid voltages sag [8] which deteriorate their robustness. The VF estimation through open loop integrators has limitations related to stability [9]. The observers based approaches presented difficulty of tuning and high computational burden. Multilayer NNs estimators proposed in [28] and [29] have a complicated structure where over ten weights are online updated. The authors in [29] have presented only real time simulation results; therefore, the proposal has not been experimentally validated. Furthermore, several strategies have not been tested for unbalanced or distorted grid voltages [6]–[9], [11], [13]–[15], [19]–[22], [24]–[26], [29]. On the other hand, complexity and high computational burden are the major drawbacks of the strategies tested under non-ideal conditions. Hence, their implementation requires expensive digital signal processors (DSPs). The cost reduction aspect is then lost. Another important consideration of sensorless operation is the startup process that guaranties smooth starting of the control algorithm. At the best of our knowledge, the startup process has not been considered in the majority of the published works.

To address the previously cited issues, this paper proposes a new sensorless control scheme of grid connected three-phase PWM rectifier that offers acceptable tradeoff between estimation accuracy and system complexity. The proposed sensorless control scheme is composed with an adaptive neural (AN) estimator for grid voltages estimation feeding a voltage-oriented control (VOC) algorithm. The AN estimator combines an adaptive neural network (ANN) to estimate the grid voltages in series with an adaptive neural filter (ANF) to improve its harmonic rejection. The simple structure of the AN estimator offers low computational burden where only three weights are online updated. This leads to easy implementation in low cost DSPs [5], [30]. In addition, its online adaptation and filtering properties ensure robustness against periodic and time-varying disturbances related to the grid voltages. The AN estimator does not depend on the control structure; therefore it can be easily adapted to different control schemes [31]. Guidelines for optimal tuning of the AN estimator's parameters are also given here in. As the control scheme needs initialization in case of sensorless operation, a new startup process is introduced to perform a simultaneous starting of the DC-link voltage and AC-line currents control loops with minimum overcurrent and reduced settling time. The evaluation of the proposed estimator is performed through simulation and experimental tests. Several working conditions are considered including unbalanced and distorted grid voltages.

This paper is organized as follows. Section II presents the design of the proposed AN estimator. The startup process and overall structure of the proposed AC voltage sensorless control strategy are described in Section III. In Section IV, a comparison between the proposed estimation method and second order generalized integrator (SOGI) based method is performed. In Section V, experimental and simulation tests are conducted to verify the feasibility and effectiveness of the proposed AN estimator. Section VI concludes this paper.

II. NNs-Based Grid Voltages Estimation

Accurate estimation of grid voltages is required for implementing a robust AC voltage sensorless control scheme. Accordingly, this section presents a novel estimation strategy based on NNs. This strategy permits to estimate online the grid voltages with low computational burden and high accuracy.

Fig. 1 describes the proposed AN estimator, which offers a reliable solution to online grid voltages estimation. It includes two simple NNs simultaneously working in series. First, an ANN is used to estimate the grid voltages. Second, an ANF is added in series for extracting fundamental components of the estimated grid voltages.

In this paper, the steepest descent and least mean square (LMS) algorithms are used for adaptive adjustment of the ANN and ANF weights, respectively. Their main advantages are low complexity, low computational demand, and high-speed convergence. Other online updating techniques like the total least squares EXIN neuron [32] or recursive least square algorithm [33] have been proposed to enhance NNs online learning capabilities. However, the use of these updating technics causes a significant increase of the complexity and computational demand of the estimator. Because this paper aims to propose a simple sensorless control scheme, steepest descent and LMS are selected as updating algorithms.

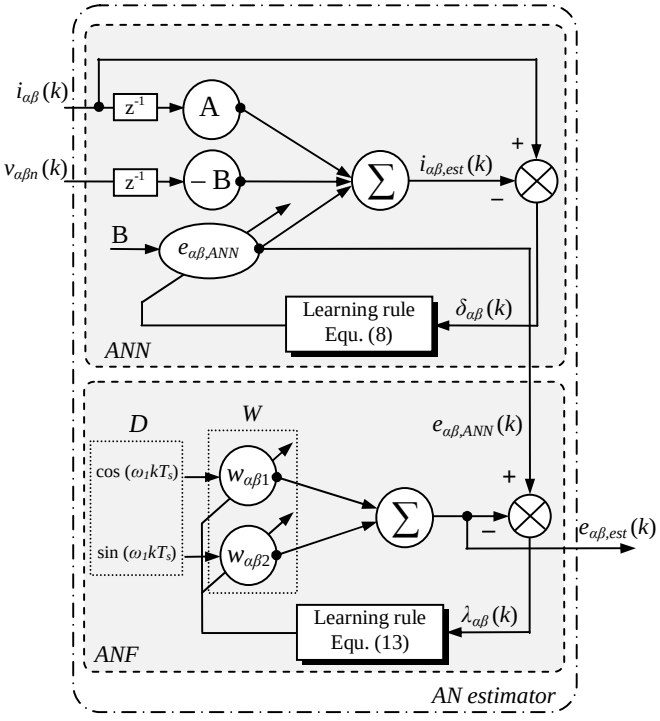

Fig. 1. Architecture of the proposed AN estimator.

A. ANN-Based Grid Voltages Estimation

The ANN topology is built from the model of the grid connected three-phase PWM rectifier shown in Fig. 2. L and R are, respectively, the inductance and resistance of the AC filter. C is the DC-link capacitance, V_{dc} is the DC-link voltage and R_L is the load resistance. i_i, v_{in} and e_i (i=a,b,c) refer to the phase-i AC-line current, input voltage and grid voltage, respectively. S_i (i=a,b,c) are the switching states of three converter legs.

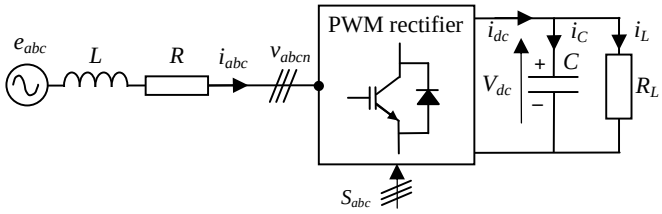

Fig. 2. Schematic diagram of the controlled three-phase PWM rectifier.

In the stationary α–β reference frame, the PWM rectifier can be modeled as follows:

$$\begin{bmatrix} e_\alpha \\ e_\beta \end{bmatrix} = L\frac{d}{dt}\begin{bmatrix} i_\alpha \\ i_\beta \end{bmatrix} + R\begin{bmatrix} i_\alpha \\ i_\beta \end{bmatrix} + \begin{bmatrix} v_{\alpha n} \\ v_{\beta n} \end{bmatrix} \tag{1}$$

where i_α, i_β, e_α and e_β are, respectively, the α- and β-axis components of the AC-line currents and the grid voltages. $v_{\alpha n}$ and $v_{\beta n}$ are the α- and β-axis components of the rectifier input voltages.

In the synchronous d–q frame, the model (1) is written as

$$\begin{bmatrix} e_d \\ e_q \end{bmatrix} = L\frac{d}{dt}\begin{bmatrix} i_d \\ i_q \end{bmatrix} + \begin{bmatrix} R & -\omega L \\ \omega L & R \end{bmatrix}\begin{bmatrix} i_d \\ i_q \end{bmatrix} + \begin{bmatrix} v_{dn} \\ v_{qn} \end{bmatrix} \tag{2}$$

where i_d, i_q, e_d and e_q are, respectively, the d- and q-axis components of the AC-line currents and the grid voltages. ω is the grid angular frequency. v_{dn} and v_{qn} are the d- and q-axis components of the rectifier input voltages.

Using the forward Euler method, the discrete-time form of (1) is obtained as follows:

$$\begin{bmatrix} i_\alpha(k) \\ i_\beta(k) \end{bmatrix} = A.\begin{bmatrix} i_\alpha(k-1) \\ i_\beta(k-1) \end{bmatrix} + B.\left(\begin{bmatrix} e_\alpha(k-1) \\ e_\beta(k-1) \end{bmatrix} - \begin{bmatrix} v_{\alpha n}(k-1) \\ v_{\beta n}(k-1) \end{bmatrix}\right) \tag{3}$$

with $\mathrm{A} = 1 - \dfrac{T_s R}{L}$ and $\mathrm{B} = \dfrac{T_s}{L}$. T_s is the sampling period.

An ANN for estimating the grid voltages (e_α, e_β) is designed using the following input/output combination:

$$\begin{bmatrix} i_{\alpha,est}(k) \\ i_{\beta,est}(k) \end{bmatrix} = A.\begin{bmatrix} i_\alpha(k-1) \\ i_\beta(k-1) \end{bmatrix} - B.\begin{bmatrix} v_{\alpha n}(k-1) \\ v_{\beta n}(k-1) \end{bmatrix} + B.\begin{bmatrix} e_{\alpha,ANN}(k-1) \\ e_{\beta,ANN}(k-1) \end{bmatrix} \tag{4}$$

where $e_{\alpha,ANN}$, $e_{\beta,ANN}$, $i_{\alpha,est}$ and $i_{\beta,est}$ are the estimated grid voltages and the ANN outputs, respectively. As can be seen from the ANN architecture presented in Fig. 1, the updated weight is the estimated grid voltages.

The weight $e_{\alpha\beta,ANN}$ is adaptively adjusted using the steepest decent algorithm by exploiting the following estimation error:

$$\begin{bmatrix} \delta_\alpha(k) \\ \delta_\beta(k) \end{bmatrix} = \begin{bmatrix} i_\alpha(k) \\ i_\beta(k) \end{bmatrix} - \begin{bmatrix} i_{\alpha,est}(k) \\ i_{\beta,est}(k) \end{bmatrix}. \tag{5}$$

Thus, a discrete-type quadratic error function can be deduced as follows:

$$E(k) = \frac{\delta_\alpha(k)^2 + \delta_\beta(k)^2}{2}. \tag{6}$$

The grid voltages are adaptively estimated by minimizing $E(k)$. For this purpose, the following Jacobian is considered [34]:

$$J = \begin{bmatrix} \dfrac{\partial E}{\partial e_{\alpha,ANN}} \\ \dfrac{\partial E}{\partial e_{\beta,ANN}} \end{bmatrix} = \begin{bmatrix} \dfrac{\partial E}{\partial i_{\alpha,est}}\dfrac{\partial i_{\alpha,est}}{\partial e_{\alpha,ANN}} \\ \dfrac{\partial E}{\partial i_{\beta,est}}\dfrac{\partial i_{\beta,est}}{\partial e_{\beta,ANN}} \end{bmatrix} = -\mathrm{B}\begin{bmatrix} i_\alpha(k) - i_{\alpha,est}(k) \\ i_\beta(k) - i_{\beta,est}(k) \end{bmatrix}. \tag{7}$$

According to the steepest descent algorithm, the weight at time (k + 1) is calculated as

$$\begin{aligned} \begin{bmatrix} e_{\alpha,ANN}(k+1) \\ e_{\beta,ANN}(k+1) \end{bmatrix} &= \begin{bmatrix} e_{\alpha,ANN}(k) \\ e_{\beta,ANN}(k) \end{bmatrix} + \begin{bmatrix} \Delta e_{\alpha,ANN}(k) \\ \Delta e_{\beta,ANN}(k) \end{bmatrix} \\ &= \begin{bmatrix} e_{\alpha,ANN}(k) \\ e_{\beta,ANN}(k) \end{bmatrix} + \mu\,\mathrm{B}\left(\begin{bmatrix} i_\alpha(k) \\ i_\beta(k) \end{bmatrix} - \begin{bmatrix} i_{\alpha,est}(k) \\ i_{\beta,est}(k) \end{bmatrix}\right) \end{aligned} \tag{8}$$

where μ is a learning rate. Therefore, the simple iterative gradient algorithm (8) is used for minimizing (7) online. It should be noticed that, under ideal condition, the ANN is sufficient for accurate grid voltages estimation. However, in case of non-ideal conditions, an additional filtering stage should be added in order to extract their fundamental components. This latter will be discussed in what follows.

B. ANF for Filtering the Estimated Grid Voltages

In this section, the estimated grid voltages $e_{\alpha\beta,ANN}$ are filtered. The time-varying magnitude and phase of the $e_{\alpha\beta,ANN}$ fundamental component are extracted using an ANF. In order to formulate this estimation problem, a suitable decomposition of $e_{\alpha\beta,ANN}$ is performed. This decomposition is given in a discrete-time as follows:

$$\begin{aligned} \begin{bmatrix} e_{\alpha,ANN}(k) \\ e_{\beta,ANN}(k) \end{bmatrix} &= \sum_{n=1}^{\infty}\left(\begin{bmatrix} E_n\cos(\omega_n k T_s + \varphi_n) \\ E_n\sin(\omega_n k T_s + \varphi_n) \end{bmatrix}\right) \\ &= \begin{bmatrix} E_1\cos(\omega_1 k T_s + \varphi_1) \\ E_1\sin(\omega_1 k T_s + \varphi_1) \end{bmatrix} + \sum_{n=2}^{\infty}\left(\begin{bmatrix} E_n\cos(\omega_n k T_s + \varphi_n) \\ E_n\sin(\omega_n k T_s + \varphi_n) \end{bmatrix}\right) \end{aligned} \tag{9}$$

with E_n is the magnitude of the n^{th} term, φ_n its initial phase angle and ω_n its pulsation. From equation (9), the fundamental component of $e_{\alpha,ANN}$ and $e_{\beta,ANN}$ can be obtained as

$$\begin{bmatrix} e_{\alpha,ANN}(k) \\ e_{\beta,ANN}(k) \end{bmatrix} = \begin{bmatrix} E_1\cos(\omega_1 k T_s + \varphi_1) \\ E_1\sin(\omega_1 k T_s + \varphi_1) \end{bmatrix}. \tag{10}$$

This can be expressed yet in the following developed form:

$$\begin{bmatrix} e_{\alpha,ANN}(k) \\ e_{\beta,ANN}(k) \end{bmatrix} = \begin{bmatrix} E_1\cos(\varphi_1)\cos(\omega_1 k T_s) - E_1\sin(\varphi_1)\sin(\omega_1 k T_s) \\ E_1\sin(\varphi_1)\cos(\omega_1 k T_s) + E_1\cos(\varphi_1)\sin(\omega_1 k T_s) \end{bmatrix}. \tag{11}$$

Form equation (11), the following vectorial notation is obtained:

$$e_{\alpha\beta,ANN}(k) = X\,D(k) \tag{12}$$

where $X = \begin{bmatrix} E_1\cos(\varphi_1) & -E_1\sin(\varphi_1) \\ E_1\sin(\varphi_1) & E_1\cos(\varphi_1) \end{bmatrix}$ and $D(k) = [\cos(\omega_1 kT_s)\ \sin(\omega_1 kT_s)]^T$.

Equation (12) is a linear combination that can be learned by one ANF with the adaptive weight $W = [w_{\alpha\beta1}\ w_{\alpha\beta2}]$. The vector $D(k)$ is represented by two generated sine waves which constitutes the ANF inputs (see Fig. 1). During the learning process, the weight W is adaptively updated to converge toward X. The weight W is updated using the LMS algorithm with the learning rate η [5], [30], [34] in the following way:

$$W(k+1) = W(k) + \frac{\eta\lambda_{\alpha\beta}(k)D(k)}{\varepsilon + D^T(k)D(k)} \tag{13}$$

where ε is a sufficiently small and positive value used to avoid division by zero if $D^T(k)D(k)=0$. $\lambda_{\alpha\beta} = e_{\alpha\beta,ANN} - e_{\alpha\beta,est}$ is the estimation error. The vector $e_{\alpha\beta,est} = [e_{\alpha,est}(k)\ e_{\beta,est}(k)]^T$ is the output of the AN estimator. It is obtained after the convergence of the ANF weight (see Fig. 1) as follows:

$$e_{\alpha\beta,est}(k) = \begin{bmatrix} e_{\alpha,est}(k) \\ e_{\beta,est}(k) \end{bmatrix} = \begin{bmatrix} E_1\cos(\omega_1 kT_s + \varphi_1) \\ E_1\sin(\omega_1 kT_s + \varphi_1) \end{bmatrix}. \tag{14}$$

C. Convergence Investigation of the AN Estimator and Learning Rates Tuning

The stability of the proposed AN estimator is investigated in this section regarding the ANN and ANF learning rates μ and η. Thus, Lyapunov's convergence criterion is exploited to establish the limits of μ and η that ensuring the AN estimator stability. The selected values of μ and η are then justified.

First, the ANN stability is analyzed. A positive definite Lyapunov function candidate for (5) is chosen and expressed as

$$V_1(k) = \frac{\delta_\alpha(k)^2 + \delta_\beta(k)^2}{2}. \tag{15}$$

The Lyapunov's convergence criterion must be satisfied such that

$$V_1(k)\Delta V_1(k) < 0 \tag{16}$$

where the Lyapunov function variation $\Delta V_1(k)$ is given by

$$\Delta V_1(k) = V_1(\delta_\alpha(k+1), \delta_\beta(k+1)) - V_1(\delta_\alpha(k), \delta_\beta(k)) < 0. \tag{17}$$

As $V_1(k)$ is a positive definite function, the stability criterion in (16) is satisfied when $\Delta V_1(k)<0$. Since the grid voltages can be considered as continuous signals and their period is much higher than the estimation period, the error variation ($\Delta\delta_\alpha(k)$, $\Delta\delta_\beta(k)$) due to the learning rate of the ANN is given as

$$\begin{aligned} \begin{bmatrix} \Delta\delta_\alpha(k) \\ \Delta\delta_\beta(k) \end{bmatrix} &= \begin{bmatrix} \delta_\alpha(k+1) \\ \delta_\beta(k+1) \end{bmatrix} - \begin{bmatrix} \delta_\alpha(k) \\ \delta_\beta(k) \end{bmatrix} \\ &= \begin{bmatrix} \frac{\partial\delta_\alpha(k)}{\partial e_{\alpha,ANN}}\Delta e_{\alpha,ANN}(k) \\ \frac{\partial\delta_\beta(k)}{\partial e_{\beta,ANN}}\Delta e_{\beta,ANN}(k) \end{bmatrix} \\ &= \mu\begin{bmatrix} \frac{\partial\delta_\alpha(k)}{\partial e_{\alpha,ANN}}\frac{\partial i_{\alpha,ANN}(k)}{\partial e_{\alpha,ANN}}\delta_\alpha(k) \\ \frac{\partial\delta_\beta(k)}{\partial e_{\beta,ANN}}\frac{\partial i_{\beta,ANN}(k)}{\partial e_{\beta,ANN}}\delta_\beta(k) \end{bmatrix} \end{aligned} \tag{18}$$

By replacing (18) in (17), $\Delta V_1(k)$ is calculated as follows:

$$\begin{aligned} \Delta V_1(k) &= \left[\Delta\delta_\alpha(k)\delta_\alpha(k) + \Delta\delta_\beta(k)\delta_\beta(k)\right] + \frac{1}{2}\left[\delta_\alpha(k)^2 + \delta_\beta(k)^2\right] \\ &= \mu\left\{\frac{\partial\delta_\alpha(k)}{\partial e_{\alpha,ANN}}\frac{\partial i_{\alpha,est}(k)}{\partial e_{\alpha,ANN}}\delta_\alpha(k)^2 + \frac{\partial\delta_\beta(k)}{\partial e_{\beta,ANN}}\frac{\partial i_{\beta,est}(k)}{\partial e_{\beta,ANN}}\delta_\beta(k)^2\right\} \\ &\quad + \frac{\mu^2}{2}\left\{\left\|\frac{\partial\delta_\alpha(k)}{\partial e_{\alpha,ANN}}\right\|^2\left\|\frac{\partial i_{\alpha,est}(k)}{\partial e_{\alpha,ANN}}\right\|^2\delta_\alpha(k)^2\right. \\ &\quad \left. + \left\|\frac{\partial\delta_\beta(k)}{\partial e_{\beta,ANN}}\right\|^2\left\|\frac{\partial i_{\beta,est}(k)}{\partial e_{\beta,ANN}}\right\|^2\delta_\beta(k)^2\right\} \end{aligned} \tag{19}$$

where $\|\cdot\|$ is the Euclidian norm in $\Re^n$. From (5) and (6), the following equality can be assumed:

$$\begin{bmatrix} \frac{\partial i_{\alpha,est}(k)}{\partial e_{\alpha,ANN}} \\ \frac{\partial i_{\beta,est}(k)}{\partial e_{\beta,ANN}} \end{bmatrix} = -\begin{bmatrix} \frac{\partial\delta_\alpha(k)}{\partial e_{\alpha,ANN}} \\ \frac{\partial\delta_\beta(k)}{\partial e_{\beta,ANN}} \end{bmatrix}. \tag{20}$$

The expression of $\Delta V_1(k)$ is obtained by replacing (20) in (19) in the following way:

$$\begin{aligned} \Delta V_1(k) &= -\mu\left\{\left\|\frac{\partial i_{\alpha,est}(k)}{\partial e_{\alpha,ANN}}\right\|^2 - \frac{\mu}{2}\left\|\frac{\partial i_{\alpha,est}(k)}{\partial e_{\alpha,ANN}}\right\|^4\right\}\delta_\alpha(k)^2 \\ &\quad - \mu\left\{\left\|\frac{\partial i_{\beta,est}(k)}{\partial e_{\beta,ANN}}\right\|^2 - \frac{\mu}{2}\left\|\frac{\partial i_{\beta,est}(k)}{\partial e_{\beta,ANN}}\right\|^4\right\}\delta_\beta(k)^2. \end{aligned} \tag{21}$$

The ANN convergence is guaranteed when the stability condition in (16) is satisfied. Hence, the learning rate μ must be selected according to the following inequality:

$$0 < \mu < \frac{2}{\max_k\left[\left\|\frac{\partial i_{\alpha,est}(k)}{\partial e_{\alpha,ANN}}\right\|^2, \left\|\frac{\partial i_{\beta,est}(k)}{\partial e_{\beta,ANN}}\right\|^2\right]}. \tag{22}$$

Secondly, the ANF stability is investigated. As the weight W computed by the ANF algorithm is an estimate of X, a positive definite Lyapunov function candidate for the ANF estimation error can be defined as

$$V_2(k) = \tilde{W}^T(k)\tilde{W}(k) \tag{23}$$

where $\tilde{\mathrm{W}}(k)$ is the ANF estimation error , defined as

$$\tilde{\mathrm{W}}(k) \equiv X(k) - \mathrm{W}(k). \tag{24}$$

The Lyapunov's convergence criterion must be satisfied such that

$$V_2(k)\Delta V_2(k) < 0 \tag{25}$$

where $\Delta V_2(k)$ is the Lyapunov function variation. As illustrated in (23), $V_2(k)$ is a positive definite function. Therefore, the stability criterion (25) is satisfied when $\Delta V_2(k) < 0$. The Lyapunov function variation is established as

$$\Delta V_2(k) = V_2\left(\tilde{\mathrm{W}}(k+1)\right) - V_2\left(\tilde{\mathrm{W}}(k)\right) < 0. \tag{26}$$

By using the ANF estimation error dynamics, obtained from (24), with the update law (13), $\Delta V_2(k)$ can be assessed as

$$\begin{aligned}\Delta V_2(k) &= \left\| \tilde{\mathrm{W}}(k) - \frac{\eta D^T(k-1) D^T(k-1) \tilde{\mathrm{W}}(k)}{\varepsilon + D^T(k-1) D(k-1)} \right\|^2 \\ &\quad - \tilde{\mathrm{W}}^T(k) \tilde{\mathrm{W}}(k) \\ &= \frac{\eta \left[\tilde{\mathrm{W}}(k) D(k-1) \right]^2}{\varepsilon + D^T(k-1) D(k-1)} \left[-2 + \frac{\eta D^T(k-1) D(k-1)}{\varepsilon + D^T(k-1) D(k-1)} \right]\end{aligned} \tag{27}$$

where $\|\cdot\|$ is the Euclidian norm in $\Re^n$. Since $\varepsilon > 0$, the stability condition in (26) is satisfied if the bracketed term in (27) is negative which means that the learning rate satisfy the inequality given below:

$$0 < \eta < 2 \tag{28}$$

The following convergence properties are also satisfied:

$$\left\| \mathrm{W}(k) - \mathrm{W}_0 \right\| \le \left\| \mathrm{W}(k-1) - \mathrm{W}_0 \right\| \le \left\| \mathrm{W}(0) - \mathrm{W}_0 \right\|, \quad k \ge 1 \tag{29.a}$$

$$\lim_{k \to \infty} \frac{\tilde{\mathrm{W}}(k) D(k-1)}{\sqrt{\varepsilon + D(k-1)^T D(k-1)}} = 0 \tag{29.b}$$

where W_0 is obtained at perfect convergence of the ANF. According to (28), the augmented error is monotonically non-increasing, hence, the convergence is guaranteed.

If the learning rates μ and η are chosen according to the intervals given by (22) and (28), respectively, the AN estimator stability is guaranteed. The μ and η values affect directly the accuracy, convergence speed and stability of the AN estimator [32]. Indeed, low values of μ and η lead to increase the accuracy and the stability at cost of slower convergence speed. On the other hand, high values of μ and η lead to high convergence speed but with less accuracy and stability. Therefore, correct choice of the learning rates is a tradeoff between the convergence speed and stability of the AN estimator.

III. Startup Process of the AC Voltage Sensorless Control Scheme

Startup procedure of control algorithms is a common problem in case of grid voltages sensorless operation of PWM rectifiers [10]. During the startup, the initial value of the grid voltages phase angle θ is needed. In case of VOC, initial values of e_d and e_q are also required. With these satisfactions, the over current can be reduced and stability of the control scheme is guaranteed.

Few startup algorithms have been proposed in the literature [19], [24], [25], [35], [36]. A common method based on the application of short zero-voltage-vector pulses at the rectifier input is proposed in [19], [24], [35]. The grid voltages angle is then deduced from the AC currents variation. However, such a technic short circuit the converters AC side. Therefore, an important over current is occurred. Extracting the initial value of θ during the diode rectifier operation mode has been also proposed in recent papers. In [36], the signs of the AC currents flowing during the diode rectifier operation are exploited to deduce an approximated value of θ using a look up table. Current signs detection based method is also proposed in [25] to detect the zero crossing interval of θ. However, both strategies start with an imprecise grid voltages position, which lead to an increased settling time. The diode rectifier operation mode (when all the IGBTs are switched off) is exploited in this paper to propose a new strategy for initial values estimation of θ, e_d and e_q at the startup. Indeed, the proposed AN estimator is applied to estimate the grid voltages by exploiting the similarity between the PWM rectifier and the diode rectifier models. Since the AN estimator needs the input voltages $v_{\alpha\beta n}$, three Heaviside functions are then used to their computation in diode rectifier operation mode. The Heaviside functions determine if the diodes are conducting or in blocking state [37]. Assuming ideal diode bridge switches, the input voltages $v_{\alpha\beta n}$ are expressed as

$$\begin{bmatrix} v_{\alpha n} \\ v_{\beta n} \end{bmatrix} = \frac{2V_{dc}}{3} \begin{bmatrix} 1 & -\frac{1}{2} & -\frac{1}{2} \\ 0 & \frac{\sqrt{3}}{2} & -\frac{\sqrt{3}}{2} \end{bmatrix} \begin{bmatrix} g_a \\ g_b \\ g_c \end{bmatrix} \tag{30}$$

where g_i = {+1 if $i_i \ge 0$; 0 if $i_i < 0$} for i=a,b,c. It should be noticed that, by replacing (30) in (1), the diode rectifier model can be obtained. Fig. 3 presents the AC-line currents and the reconstructed input voltages from (30) during diode rectifier operation mode.

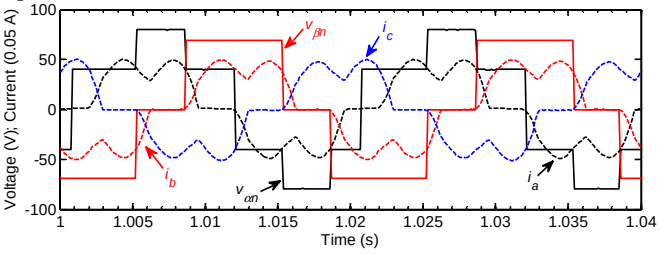

Fig. 3. Sensed AC-line currents (i_a, i_b and i_c) and computed input voltages ($v_{\alpha n}$ and $v_{\beta n}$) during diode rectifier operation mode (experiment).

The overall sensorless control scheme is depicted in Fig. 4. It consists of a control unit and an estimation unit. The control unit based on VOC maintains a constant DC-link voltage under a UPF operation [5]. The estimated parameters θ_{est}, $e_{d,est}$ and $e_{q,est}$ are obtained from the AN estimator through a phase locked loop (PLL). The estimation unit ensures grid voltages estimation and a smooth starting of the VOC. The equation (30) is used to compute the input voltages during the diode rectifier operation mode. The obtained input voltages are

injected in the AN estimator. Thus, the grid voltages are accurately estimated under diode rectifier operation. Thereafter, the estimated grid voltages are used in a PLL to obtain initial values of θ, e_d and e_q. The VOC is finally started and initialized by the PLL outputs (θ_{est}, $e_{d,est}$ and $e_{q,est}$). Simultaneously, the input voltages obtained from (30) are switched to the actual input voltages (see Fig. 4). Note that, in PWM operation mode, the actual input voltages are obtained from the current controller outputs. This leads to avoiding direct measurements that are affected by the modulation and acquisition noise [7], [28].

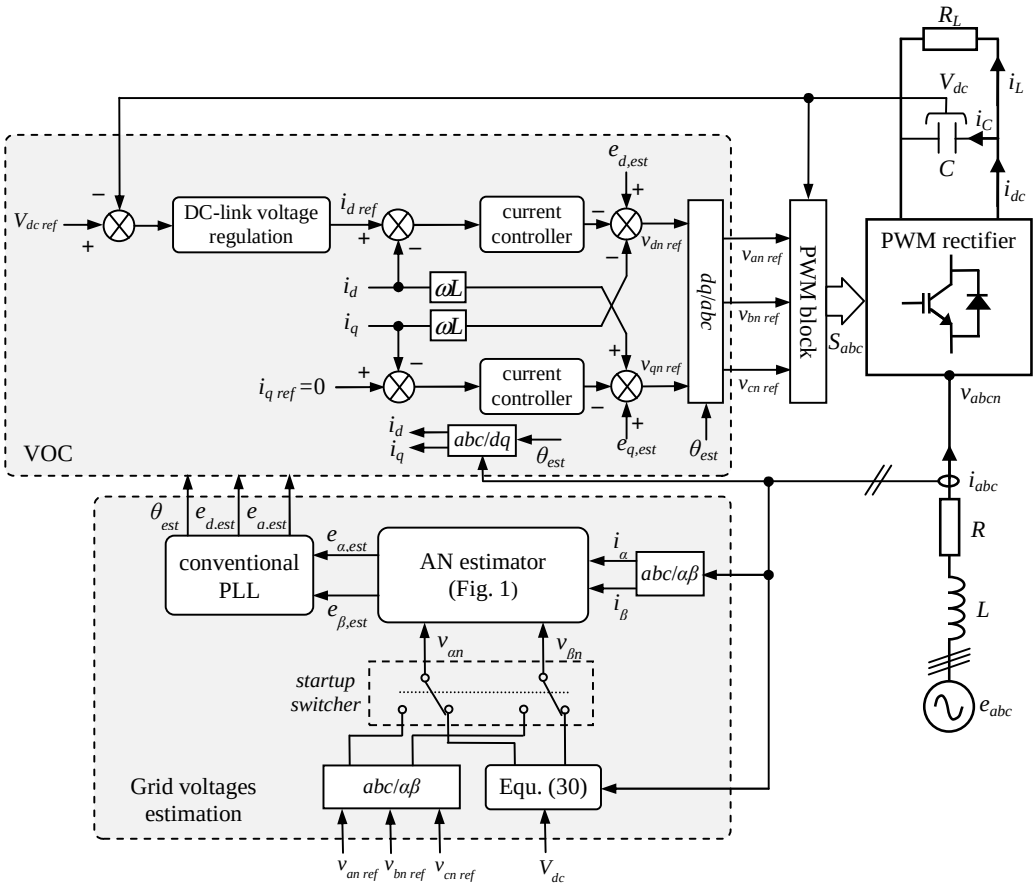

Fig. 4. Overall structure of the developed AC voltage sensorless control.

IV. Comparison Between the Proposed Estimation Method and SOGI Based Estimation Method

To prove the superiority of the proposed AC voltage sensorless control algorithm, comparative study between the AN estimator and the recently developed SOGI based estimation method [9], [10] has been performed. First, the SOGI method is presented. Thereafter, simulation tests are carried out in MATLAB/Simulink environment.

The SOGI based estimation method uses the VF concept where a virtual AC motor is assumed from the behavior of the grid voltages and the AC filter. Then, the grid voltages are induced by a virtual magnetic flux [9], [10], [17]. In α–β reference frame, the VF $\phi_{\alpha\beta}$ can be estimated from the integration of the grid voltages as follows:

$$\phi_{\alpha\beta} = \int e_{\alpha\beta}\, dt = Li_{\alpha\beta} + \phi_{\alpha\beta n} \tag{31}$$

where $\phi_{\alpha\beta n} = \int \left(v_{\alpha\beta n} + Ri_{\alpha\beta}\right) dt$.

The integration in (31) induces saturation and DC offset in the estimated VF. To overcome this, the authors in [9] and [10] proposed a SOGI based adaptive filter with a cutoff frequency ω. The SOGI transfer function is given by

$$F(s) = \frac{\phi_{\alpha\beta nf}(s)}{\phi_{\alpha\beta n}(s)} = \frac{k_e \omega s}{s^2 + k_e \omega s + \omega^2} \tag{32}$$

where $\phi_{\alpha\beta nf}$ is the filtered quantity of $\phi_{\alpha\beta n}$ and k_e is a parameter that influences the SOGI filter speed convergence. Note that since no grid voltages information is available from the SOGI method, the estimated VF is utilized to derive the estimated grid voltages used in VOC control scheme [20]. This is performed in the following way:

$$\begin{bmatrix} e_{\alpha,est} \\ e_{\beta,est} \end{bmatrix} = \begin{bmatrix} -\omega\phi_\beta \\ \omega\phi_\alpha \end{bmatrix}. \tag{33}$$

In the present comparative study, k_e is optimally tuned according to [38] and the AN estimator learning rates (μ, η) are tuned according to the criterions established in Section II-C. Thus, both the AN estimator and the SOGI based estimator are tuned to their best. To perform the comparison, the two estimation methods are simulated in the same conditions where two tests are carried out. The simulation parameters are summarized in Table I.

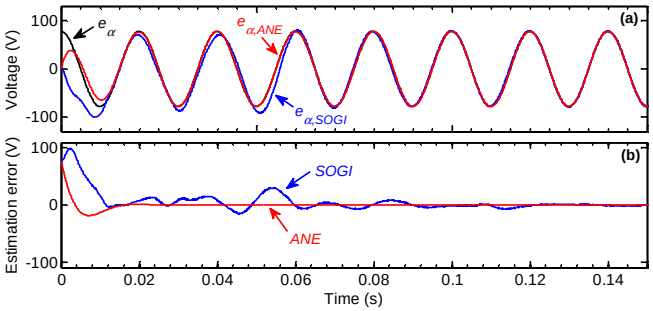

Fig. 5. Comparison between the AN estimator and the SOGI estimator at startup (simulation): (a) actual grid voltage e_α and estimated grid voltages ($e_{\alpha,ANE}$, $e_{\alpha,SOGI}$), (b) estimation errors.

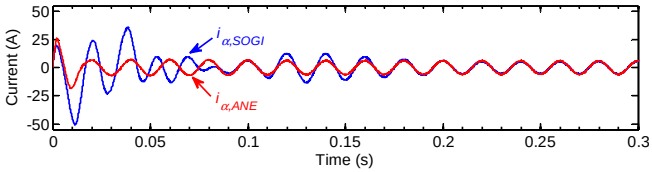

Fig. 6. Actual AC-line currents $i_{\alpha,ANE}$ and $i_{\alpha,SOGI}$ when the control methods based on the AN estimator and the SOGI estimator are used (simulation).

Performances comparison between the AN estimator and the SOGI based estimator in term of tracking speed of the grid voltages is illustrated in Fig. 5. In this simulation, R_L is set to 55Ω and $V_{dc\ ref}$ is fixed to 190 V. Both estimators are started without initialization. Fig. 5(a) shows the actual grid voltage e_α and its estimations $e_{\alpha,ANE}$ and $e_{\alpha,SOGI}$ provided by the AN estimator and the SOGI based estimator, respectively. In Fig. 5(b) the corresponding estimation errors are presented. These results show that, compared to the SOGI based estimator, the AN estimator exhibits faster convergence and low estimation error. Fig. 6 illustrates the actual AC-line currents $i_{\alpha,ANE}$ and $i_{\alpha,SOGI}$ corresponding to the sensorless control methods based on AN estimator and the SOGI based estimator, respectively. From this result, it is clear that the control method based SOGI estimator causes higher overshoots and longer settling time. Furthermore, this test shows the necessity of using initial values of the grid voltages at the startup.

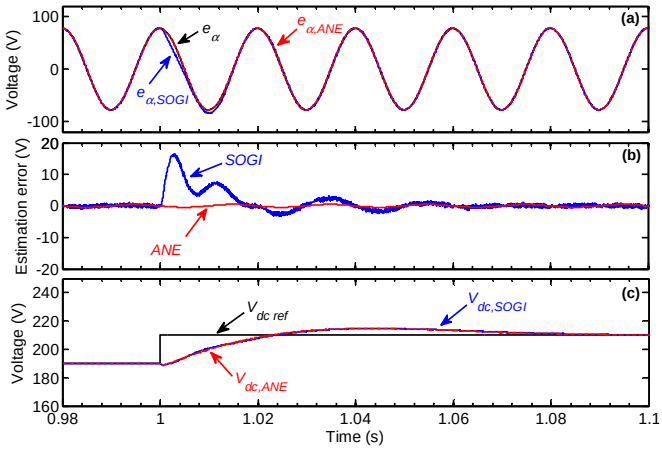

Fig. 7. Performances comparison under $V_{dc\ ref}$ step change (simulation): (a) actual grid voltage e_α and estimated grid voltages ($e_{\alpha,ANE}$, $e_{\alpha,SOGI}$), (b) estimation errors and (c) reference DC-link voltage $V_{dc\ ref}$ and measured DC-link voltages ($V_{dc,ANE}$, $V_{dc,SOGI}$).

Performances comparison between the control methods based on AN estimator and SOGI estimator under $V_{dc\ ref}$ step change is given in Fig. 7. In this test, R_L is set to 55Ω. At time t=1s, a step change of 20V in $V_{dc\ ref}$ is applied ($V_{dc\ ref}$ passes from 190V to 210V). The actual grid voltage e_α and the estimated voltages $e_{\alpha,ANE}$ and $e_{\alpha,SOGI}$ are shown in Fig. 7(a). The corresponding estimation errors are illustrated in Fig. 7(b). From these figures, it is clear that the AN estimator is not affected by $V_{dc\ ref}$ step change unlike the SOGI estimator where an estimation error has occurred. This is mainly due to the SOGI filter which is not applied to the whole estimated flux. As shown in (31) and (32), the current through L is not filtered. Indeed, in transient phase, the SOGI estimator may lose information of $Li_{\alpha\beta}$ being not sinusoidal or having a different frequency than ω. However, in our proposed estimation method, all the quantities used in the estimation are processed by the AN estimator. This leads to robust estimation during $V_{dc\ ref}$ step change. Controlled DC-Link voltages corresponding to each estimation strategy are presented in Fig. 7(c). It can be observed that the DC-Link voltages follow correctly $V_{dc\ ref}$.

From the obtained results, the AN estimator presented faster convergence and better accuracy compared to the SOGI based estimator. In order to verify the feasibility, robustness and accuracy of the proposed AC voltage sensorless control scheme, experimental and simulation tests are carried out in the following section.

V. Results

The laboratory setup used for experimenting the developed AC voltage sensorless control algorithm, illustrated in Fig. 4, is presented in Fig. 8. It consists of a three-phase insulate-gate-bipolar-transistor based PWM rectifier with anti-paralleling diodes. Two current sensors and one voltage sensor are used to measure two input currents (i_a and i_b) and DC-link voltage V_{dc}, respectively. It should be noted that, three voltage sensors are used for measuring the grid voltages. These measured voltages are not used in the closed-loop control scheme. Therefore, they are only used to perform comparison between the estimated grid voltages and the actual ones. The developed AC voltage sensorless control algorithm is implemented in MATLAB-Simulink environment and executed on a dSPACE DS1104 board using Euler resolution method. The experimental platform specifications can be found in Table I.

TABLE I
System Parameters

Parameter	Simulation	Experiment
Nominal DC-link voltage (V)	190	190
Phase grid voltage rms (V)	55	55
Grid voltages frequency f (Hz)	50	50
Nominal AC filter resistance R (Ω)	1	1
Nominal AC filter resistance L (mH)	8	8
DC-link capacitor C (mF)	3.3	3.3
Load resistance R_L (Ω)	55	55
Sampling time (µs)	10	110
Switching frequency (kHz)	7.5	7.5

The AN estimator is implemented with the learning rates

μ=9520 and η=0.04 which are experimentally adjusted to ensure stability and optimal convergence speed according to the criterions established in section II-C. Thus, these learning rate values are both used in simulation and experiment tests. During all tests, the PWM rectifier operates at UPF since the current $i_{q\ ref}$ is fixed to zero.

In the following subsections, experimental (from Fig. 9 to Fig. 20) and simulation (Figs. 21 and 22) tests are carried out. The AN estimator is experimentally tested in different operating conditions such as diode rectifier operation mode, startup process, $V_{dc\ ref}$ variation, R_L variation, symmetrical grid voltages sag and unbalanced grid voltages. Finally, the AN estimator is simulated under distorted grid voltages. The simulation test is done in a MATLAB-Simulink environment using the parameters listed in Table I.

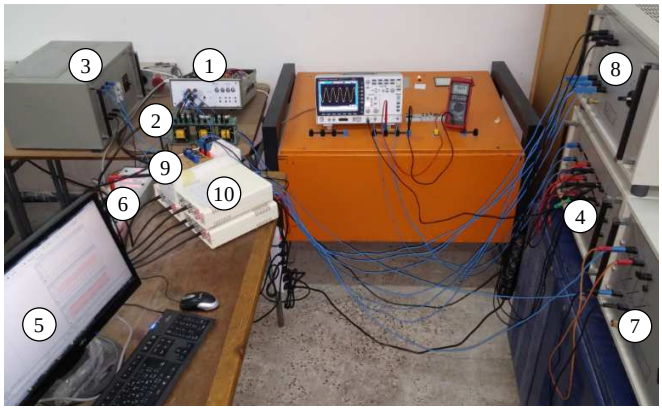

Fig. 8. Photograph of the implemented test bench: 1) three-phase PWM rectifier, 2) interconnecting inductances, 3) interconnecting resistances, 4) isolating transformer, 5) PC-Pentium + dSPACE board + ControlDesk, 6) dSPACE input/output connectors, 7) load resistance, 8) additional resistances, 9) current sensors, 10) voltage sensors.

A. Performances of the AN estimator in Diode Rectifier Operation Mode

Experimental results of the grid voltages estimation in diode rectifier operation mode are presented in Figs. 9 and 10. In this experiment, the load resistance is set to 55 Ω. So, the DC-link voltage is around 117 V. Figs. 9(a) and 9(b) illustrate the signals used as inputs of the AN estimator. The input voltages ($v_{\alpha n}$, $v_{\beta n}$) are obtained from (30). From Fig. 9(c) and 9(d), the $\alpha\beta$-axes components of the grid voltages are accurately estimated. After the estimation process, $e_{\alpha,est}$ and $e_{\beta,est}$ are inserted in the PLL (see Fig. 4). In Fig. 10, the estimated dq-axes components ($e_{d,est}$, $e_{q,est}$) and the phase angle (θ_{est}) of the grid voltages are illustrated. Therefore, the estimated quantities ($e_{d,est}$, $e_{q,est}$ and θ_{est}) will be used as initial values in order to achieve smooth startup of the sensorless control scheme.

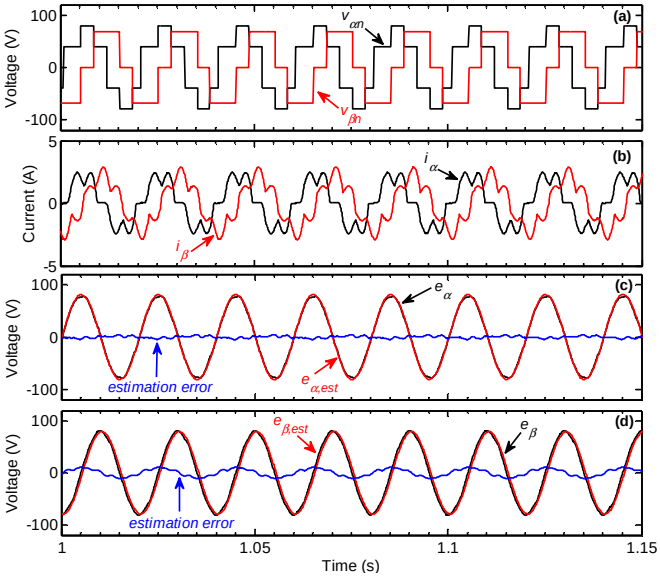

Fig. 9. Steady-state performances of the AN estimator in diode rectifier operation mode (experiment): (a) computed input voltages $v_{\alpha n}$ and $v_{\beta n}$, (b) actual AC-line currents i_α and i_β, (c) actual grid voltage e_α, estimated grid voltage $e_{\alpha,est}$ and estimation error and (d) actual grid voltage e_β, estimated grid voltage $e_{\beta,est}$ and estimation error.

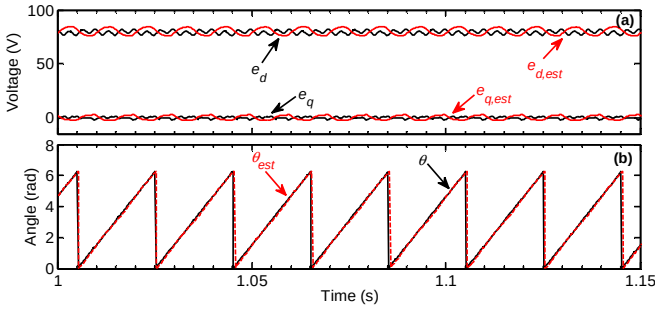

Fig. 10. Steady-state performances of the PLL in diode rectifier operation mode (experiment): (a) computed dq components (e_d, e_q) with actual grid voltages and computed dq components ($e_{d,est}$, $e_{q,est}$) with estimated grid voltages and (b) computed angles θ and θ_{est} with actual and estimated grid voltages, respectively.

B. Startup Process

Figs. 11 and 12 present obtained experimental results of the proposed sensorless control strategy at startup. In this experiment, $V_{dc\ ref}$ is fixed to 190 V and R_L is set to 55 Ω. The input voltages $v_{\alpha n}$ and $v_{\beta n}$ are shown in Fig. 11(a). The VOC strategy is started at t = 1.34s. Simultaneously, the input voltages computed from (30) are switched to $\alpha\beta$-axes components of the current controller outputs ($v_{\alpha n\ ref}$ and $v_{\beta n\ ref}$) (see Fig. 4). As illustrated in Figs. 11(b) and (c), the proposed startup process prevents the over-current trip and reduces the commissioning time of the controlled system. So, V_{dc} rapidly follows its reference. It passes from 117V to 190V in about 0.1s. This settling time is due to the time constant of the external control loop. The actual and estimated grid voltages are shown in Fig. 11(d) and (e). It is clear that the estimated voltages are close to the actual ones and present a minimum estimation error at startup. For comparison purpose, two PLLs are computed with actual and estimated grid voltages. The obtained results are presented in Fig. 12. Reduced oscillations and noises are obtained from the PLL computed with

estimated grid voltages. The actual phase angle is also accurately tracked. Consequently, this experiment prove that the AN estimator can successfully estimates the grid voltages. The stability of the sensorless control strategy is also guaranteed at startup.

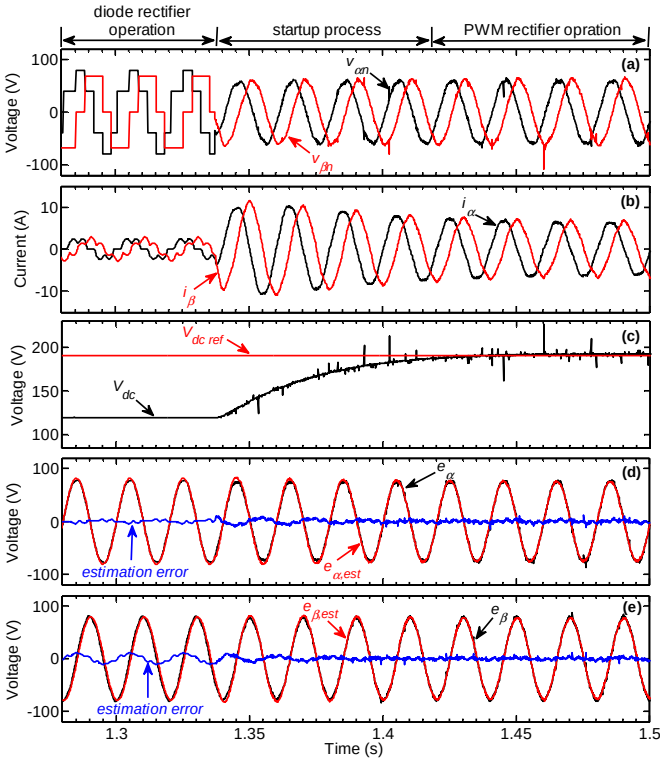

Fig. 11. Performances of the AN estimator at startup (experiment): (a) input voltages v_{an} and $v_{\beta n}$, (b) actual AC-line currents i_α and i_β, (c) reference and measured DC-link voltages ($V_{dc\ ref}$, V_{dc}), (d) actual grid voltage e_α, estimated grid voltage $e_{\alpha,est}$ and estimation error and (d) actual grid voltage e_β, estimated grid voltage $e_{\beta,est}$ and estimation error.

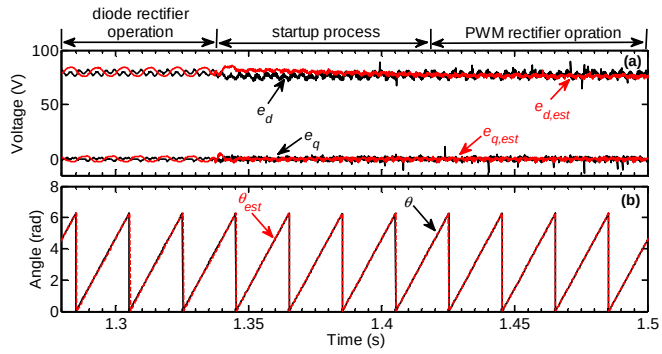

Fig. 12. Performances of the PLL at startup (experiment): (a) computed dq components (e_d, e_q) with actual grid voltages and computed dq components ($e_{d,est}$, $e_{q,est}$) with estimated grid voltages and (b) computed angles θ and θ_{est} with actual and estimated grid voltages, respectively.

C. Robustness Analysis

To verify the robustness of the proposed sensorless control strategy several tests have been conducted under different working conditions. The results are given in Figs. 13–22.

1) $V_{dc\ ref}$ variation: In this experiment, R_L is set to 55Ω. A step change of 20V in $V_{dc\ ref}$ is applied at t = 1.287 s ($V_{dc\ ref}$ passes from 190V to 210V). As shown in Fig. 13(a) and (b), the actual and estimated grid voltages are superimposed. During the step change in $V_{dc\ \mathrm{ref}}$, the currents rise from 6A to 8A (see Fig. 13(c)). This increases the flowed power from the AC side to the DC side. V_{dc} is given in Fig. 13(d). It follows accurately its reference before and after the step change. From Fig. 14, the PLL gives great performances with the estimated grid voltages where the computed quantities are not affected by the $V_{dc\ ref}$ step change. The actual phase angle is also well tracked.

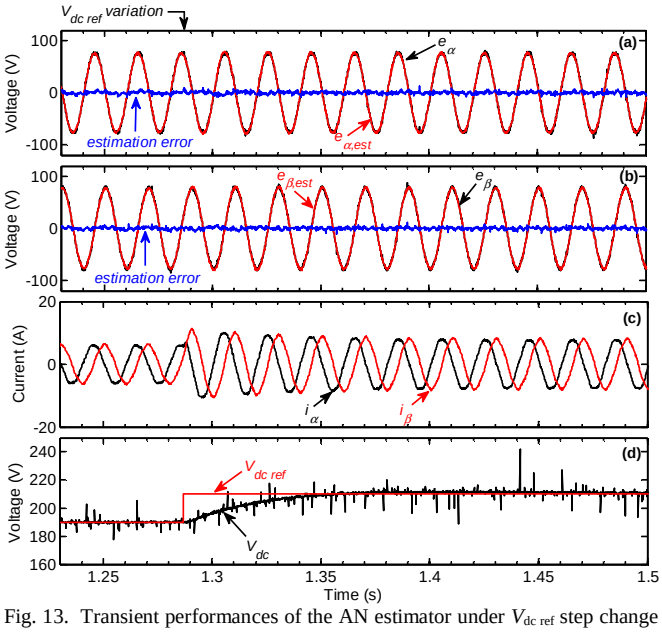

Fig. 13. Transient performances of the AN estimator under $V_{\mathrm{dc\ ref}}$ step change (experiment): (a) actual grid voltage e_α, estimated grid voltage $e_{\alpha,est}$ and estimation error, (b) actual grid voltage e_β, estimated grid voltage $e_{\beta,est}$ and estimation error, (c) actual AC-line currents i_α and i_β and (d) reference and measured DC-link voltages.

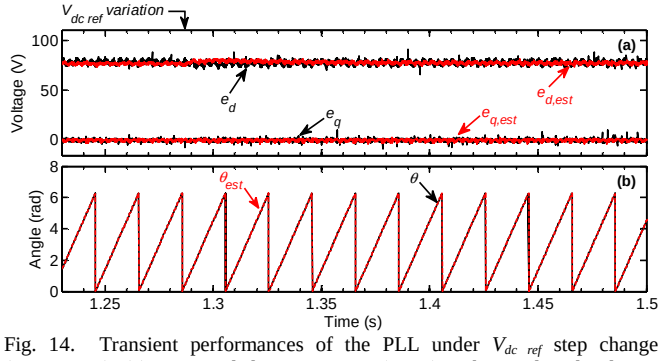

Fig. 14. Transient performances of the PLL under $V_{dc\ ref}$ step change (experiment): (a) computed dq components (e_d, e_q) with actual grid voltages and computed dq components ($e_{d,est}$, $e_{q,est}$) with estimated grid voltages and (b) computed angles θ and θ_{est} with actual and estimated grid voltages, respectively.

2) Load resistance variation: In this test, a variation of 35% in R_L is applied during 0.23s. $V_{\mathrm{dc\ ref}}$ is fixed to 190V. In Figs. 15(a) and (b), the actual grid voltages are well tracked with low estimation errors. Thus, R_L variation seems not affect the estimation algorithm. From Fig. 15(c), the currents vary from 6A to 10A. Transient performances of the PLL are shown in Fig. 16. Actually, the PLL provides good performances with the estimated grid voltages. The actual phase angle remains well tracked.

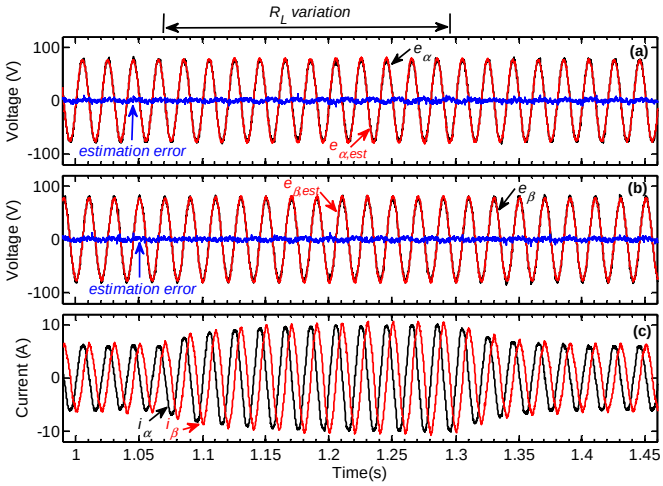

Fig. 15. Transient performances of the AN estimator under load resistance variation (experiment): (a) actual grid voltage e_α, estimated grid voltage $e_{\alpha,est}$ and estimation error, (b) actual grid voltage e_β, estimated grid voltage $e_{\beta,est}$ and estimation error and (c) actual AC-line currents.

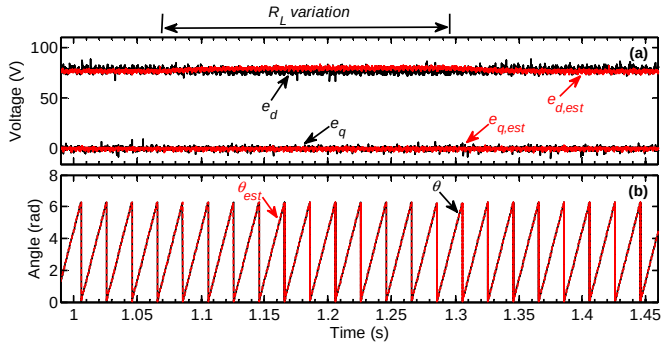

Fig. 16. Transient performances of the PLL under load resistance variation (experiment): (a) computed dq components (e_d, e_q) with actual grid voltages and computed dq components ($e_{d,est}$, $e_{q,est}$) with estimated grid voltages and (b) computed angles θ and θ_{est} with actual and estimated grid voltages, respectively.

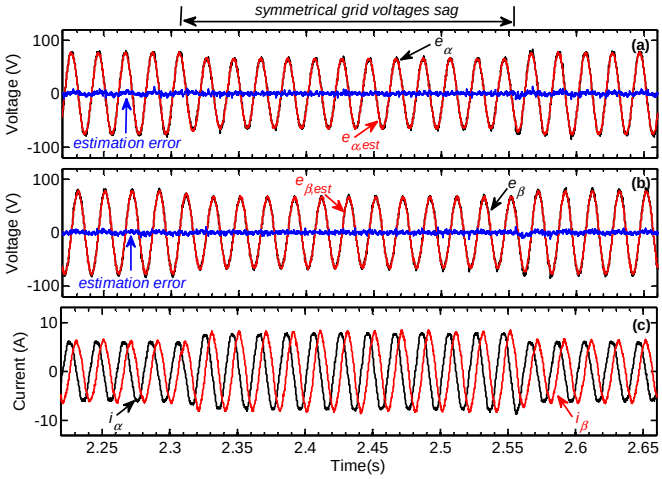

Fig. 17. Transient performances of the AN estimator under symmetric grid voltages sag (experiment): (a) actual grid voltage e_α, estimated grid voltage $e_{\alpha,est}$ and estimation error and (b) actual grid voltage e_β, estimated grid voltage $e_{\beta,est}$ and estimation error and (c) actual AC-line currents.

3) Symmetrical grid voltages sag: In this experiment, $V_{dc\ ref}$ is fixed to 190V and R_L is set to 55Ω. Symmetrical grid voltages sag of 16% is applied during 0.25s by adding three-phase resistance of 1.5Ω in the AC side (see Fig. 8). As shown in Fig. 17, the AN estimator stability is ensured and the grid voltages are rapidly estimated during the symmetrical grid voltages sag. An increase in the AC-line currents due to the power flow variation is observed during the sag. In Fig. 18, transient performances of the PLL are presented under symmetrical grid voltages sag. The dq-axes components of the grid voltages and phase angle are well estimated.

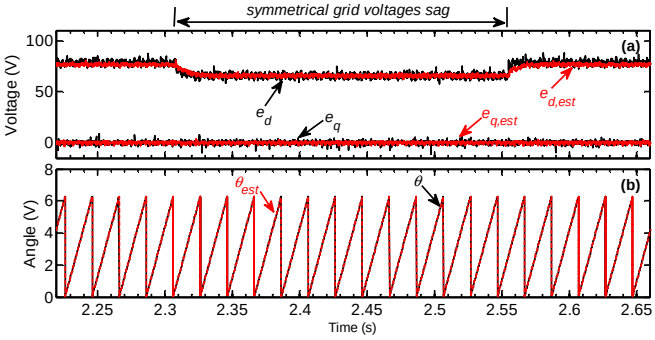

Fig. 18. Transient performances of the PLL under symmetric grid voltages sag (experiment): (a) computed dq components (e_d, e_q) with actual grid voltages and computed dq components ($e_{d,est}$, $e_{q,est}$) with estimated grid voltages and (b) computed angles θ and θ_{est} with actual and estimated grid voltages, respectively.

4) Unbalanced grid voltages: In this experiment, $V_{dc\ ref}$ is maintained to 190V and R_L is set to 55Ω. Two-phase sag is applied during 0.25s. As presented in Fig. 19(a) and (b), the AN estimator is not affected by the grid voltage unbalance. The estimation error remains very close to zero. Fig. 19(c) shows the currents i_α and i_β. Although grid voltage unbalance causes AC-line currents distortion, a stable operation of the overall control strategy is guaranteed. Clearly, the computed components with actual and estimated grid voltages shown in Fig. 20 are distorted. This is only due to limitation of the used PLL against unbalanced conditions. Therefore, it cannot be considered as an issue of the proposed estimation strategy.

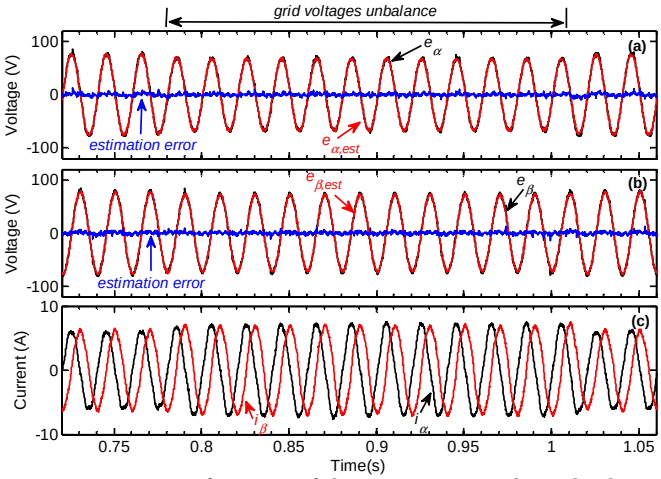

Fig. 19. Transient performances of the AN estimator under grid voltages unbalance (experiment): (a) actual grid voltage e_α, estimated grid voltage $e_{\alpha,est}$ and estimation error and (b) actual grid voltage e_β, estimated grid voltage $e_{\beta,est}$ and estimation error and (c) actual AC-line currents.

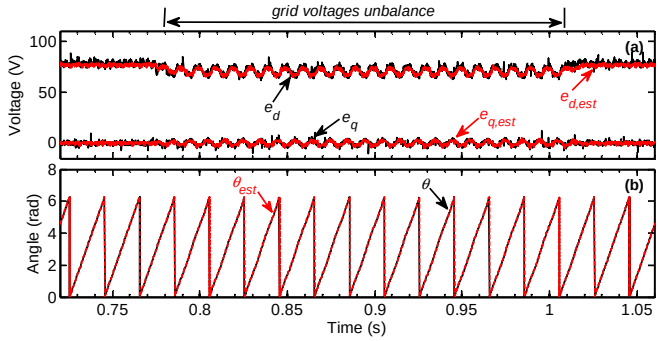

Fig. 20. Transient performances of the PLL under grid voltages unbalance (experiment): computed *dq* components (e_d, e_q) with actual grid voltages and computed *dq* components ($e_{d,est}$, $e_{q,est}$) with estimated grid voltages and (b) computed angles θ and θ_{est} with actual and estimated grid voltages, respectively.

5) Distorted grid voltages: In this simulation, R_L is set to 55Ω, $V_{dc\ ref}$ is fixed to 190V and the grid voltages contain the 5th and 7th harmonic components (5% of the 5th harmonic and 5% of the 7th harmonic). As can be seen from Figs. 21(a) and (b), the estimated voltages are well filtered without any influence of the actual grid voltages distortion on the estimation process. This is due to the ANF designed at the fundamental grid voltages frequency. This leads to fundamental components estimation of the grid voltages even under distorted conditions. It should be mentioned that the distortions observed in i_α and i_β (see Fig. 21(c)) are caused by the used current controllers (simple PI controllers) and not by the AN estimator. Fig. 22 shows performances of the PLL. The computed quantities (e_d, e_q and θ) using the actual grid voltages present large ripples which are due to the limited PLL performances against harmonic distortions. As the distortions do not appear on the estimated grid voltages, the quantities ($e_{d,est}$, $e_{q,est}$ and θ_{est}) do not present significant oscillations.

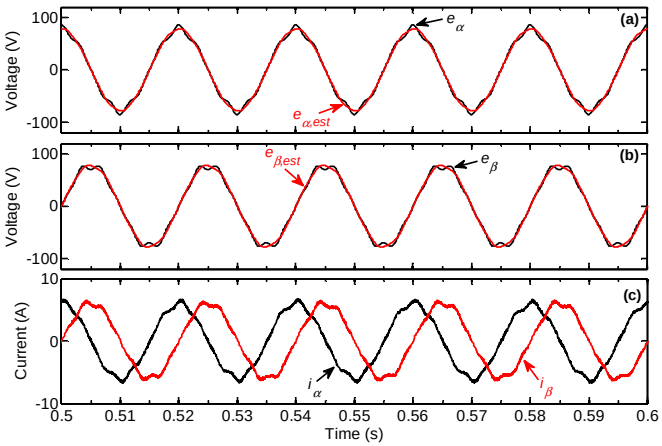

Fig. 21. Transient performances of the AN estimator under distorted grid voltages (simulation): (a) actual grid voltage e_α and estimated grid voltage $e_{\alpha,est}$, (b) actual grid voltage e_β and estimated grid voltage $e_{\beta,est}$ and (c) actual AC-line currents.

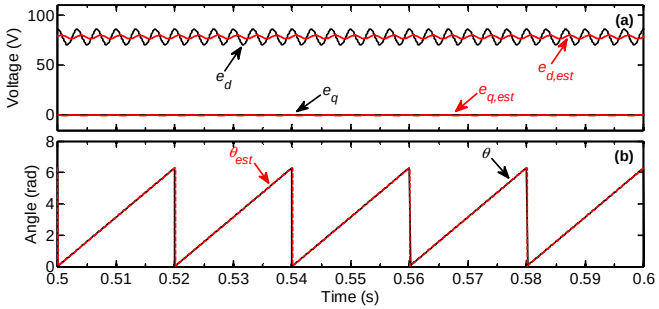

Fig. 22. Transient performances of the PLL under distorted grid voltages (simulation): computed *dq* components (e_d, e_q) with actual grid voltages and computed *dq* components ($e_{d,est}$, $e_{q,est}$) with estimated grid voltages and (b) computed angles θ and θ_{est} with actual and estimated grid voltages respectively.

VI. Conclusion

In this work, a new AN estimator for eliminating the grid voltage sensors in VOC of three-phase PWM rectifier has been proposed. The developed AN estimator combines estimation capability of the ANN and filtering property of the ANF. Lyapunov's theory based stability analysis has been exploited for optimal tuning of the AN estimator. Hence, simple, accurate and fast grid voltages estimation has been obtained. To avoid current overshoot and to reduce the settling time at the startup, a new startup process has been proposed to initialize the VOC. The effectiveness of the proposed procedure has been experimentally demonstrated. A comparison between the proposed AN estimator and the recently developed SOGI based estimator has been conducted. This comparison has clearly indicated faster convergence and better accuracy of the proposed estimator. Finally, robustness of the AN estimator regarding to step change in DC-link voltage reference, load resistance variation and non-ideal grid voltages conditions (symmetrical sag, unbalance, distortion) has been investigated through simulation and experimental tests. The obtained results have demonstrated high performances of the proposed AN estimator within the analyzed working conditions.

References

[1] R. Teodorescu, M. Liserre, and P. Rodriguez, *Grid converters for photovoltaic and wind power systems*, John Wiley & Sons, 2011.

[2] A.-R. Haitham, M. Malinowski, and K. Al-Haddad, *Power electronics for renewable energy systems, transportation and industrial applications*, John Wiley & Sons, 2014.

[3] T. Friedli, M. Hartmann, and J. W. Kolar, "The essence of three-phase PFC rectifier systems–Parte II," *IEEE Trans. Power Electron.*, vol. 29, no. 2, pp. 543–560, Feb. 2014.

[4] M. B. Ketzer and C. B. Jacobina, "Sensorless control technique for PWM rectifiers with voltage disturbance rejection and adaptive power factor," *IEEE Trans. Ind. Electron.*, vol. 62, no. 2, pp. 1140–1151, Feb. 2015.

[5] A. Bechouche, H. Seddiki, D. Ould Abdeslam, and K. Mesbah, "Adaptive AC filter parameters identification for voltage-oriented control of three-phase voltage-source rectifiers", *Int. J. Modell. Identification Control*, vol. 24, no. 4, pp. 319–331, 2015.

[6] H. Gholami-Khesht, M. Monfared, and S. Golestan, "Low computational burden grid voltage estimation for grid connected voltage source converter-based power applications," *IET Power Electron.*, vol. 8, no. 5, pp. 656–664, Apr. 2015.

[7] H. Gholami-Khesht and M. Monfared, "Novel grid voltage estimation by means of the Newton–Raphson optimisation for three-phase grid connected voltage source converters," *IET Power Electron.*, vol. 7, no. 12, pp. 2945–2953, Dec. 2014.

[8] A. A. Ghodke and K. Chatterjee, "One-cycle-controlled bidirectional three-phase unity power factor ac–dc converter without having voltage sensors," *IET Power Electron.*, vol. 5, no. 9, pp. 1944–1955, Nov. 2012.

[9] M. B. Ketzer and C. B. Jacobina, "Virtual flux sensorless control for shunt active power filters with quasi-resonant compensators," *IEEE Trans. Power Electron.*, vol. 31, no. 7, pp. 4818–4830, July 2016.

[10] J. A. Suul, A. Luna, P. Rodriguez, and T. Undeland, "Virtual-flux-based voltage-sensor-less power control for unbalanced grid conditions," *IEEE Trans. Power Electron.*, vol. 27, no. 9, pp. 4071–4087, Sept. 2012.

[11] S. G. Jorge, C. A. Busada, and J. Solsona, "Low computational burden grid voltage sensorless current controller," *IET Power Electron.*, vol. 6, no. 8, pp. 1592–1599, Sept. 2013.

[12] J. Kukkola and M. Hinkkanen, "State observer for grid-voltage sensorless control of a converter equipped with an LCL filter: direct discrete-time design," *IEEE Trans. Ind. Appl.* vol. 52, no. 4, pp. 3133–3145, July/Aug. 2016.

[13] A. Mallik and A. Khaligh,, "Control of a three-phase boost PFC converter using a single DC link voltage sensor," *IEEE Trans. Power Electron.*, DOI: 10.1109/TPEL.2016.2614769, 2016.

[14] K.-J. Lee, B.-G. Park, R.-Y. Kim, and D.-S. Hyun, "Robust predictive current controller based on a disturbance estimator in a three-phase grid-connected inverter," *IEEE Trans. Power Electron.*, vol. 27, no. 1, pp. 276–283, Jan. 2012.

[15] T. Noguchi, H. Tomiki, S. Kondo, and I. Takahashi, "Direct power control of PWM converter without power-source voltage sensors," *IEEE Trans. Ind. Appl.*, vol. 34, no. 3, pp. 473–479, May/June 1998.

[16] Y. Cho and K.-B. Lee, "Virtual-flux-based predictive direct power control of three-phase PWM rectifiers with fast dynamic response," *IEEE Trans. Power Electron.*, vol. 31, no. 4, pp. 3348–3359, Apr. 2016.

[17] J. G. Norniella, J. M. Cano, G. A. Orcajo, C. H. Rojas, J. F. Pedrayes, M. F. Cabanas, and M. G. Melero, "Improving the dynamics of virtual-flux-based control of three-phase active rectifiers," *IEEE Trans. Ind. Electron.*, vol. 61, no. 1, pp. 177–187, Jan. 2014.

[18] A. M. Razali, M. A. Rahman, G. George, and N. A. Rahim, "Analysis and design of new switching lookup table for virtual flux direct power control of grid-connected three-phase PWM AC–DC converter," *IEEE Trans. Ind. Appl.*, vol. 51, no. 2, pp. 1189–1200, March/April 2015.

[19] A. Kulka, "Sensorless digital control of grid connected three phase converters for renewable sources," Ph.D. dissertation, Norwegian Univ. Sci. Technol., Trondheim, Norway, 2009.

[20] Z. Zhang, H. Xu, M. Xue, Z. Chen, T. Sun, R. Kennel, and C. M. Hackl, "Predictive control with novel virtual-flux estimation for back-to-back power converters," *IEEE Trans. Ind. Electron.*, vol. 62, no. 5, pp. 2823–2834, May 2015.

[21] Y. Tao, Q. Wu, L. Wang, and W. Tang, "Voltage sensorless predictive direct power control of three-phase PWM converters," *IET Power Electron.*, vol. 9, no. 5, pp. 1009–1018, Apr. 2016.

[22] K. H. Ahmed, A. M. Massoud, S. J. Finney, and B. W. Williams, "Sensorless current control of three-phase inverter-based distributed generation," *IEEE Trans. Power Del.*, vol. 24, no. 2, pp. 919–929, Apr. 2009.

[23] R. Guzman, L. G. de Vicuña, J. Morales, M. Castilla, and J. Miret, "Model-based control for a three-phase shunt active power filter," *IEEE Trans. Ind. Electron.*, vol. 63, no. 7, pp. 3998–4007, July. 2016.

[24] H. Yoo, J.-H. Kim, and S.-K. Sul, "Sensorless operation of a PWM rectifier for a distributed generation," *IEEE Trans. Power Electron.*, vol. 22, no. 3, pp. 1014–1018, May 2007.

[25] T. Liu, C. Xia, and T. Shi, "Robust model predictive current control of grid-connected converter without alternating current voltage sensors," *IET Power Electron.*, vol. 7, no. 12, pp. 2934–2944, Dec. 2014.

[26] H. Gholami-Khesht and M. Monfared, "Deadbeat direct power control for grid connected inverters using a full-order observer," *3rd Int. Conf. Electr. Power Energy Convers. Syst. (EPECS)*, Nov. 2015, pp. 1–5.

[27] J. Kukkola, M. Hinkkanen, and K. Zenger, "Observer-Based State-Space Current Controller for a Grid Converter Equipped With an LCL Filter: Analytical Method for Direct Discrete-Time Design," *IEEE Trans. Ind. Appl.*, vol. 51, no. 5, pp. 4079–4090, 2015.

[28] Y. A.-R. I. Mohamed and E. F. El-Saadany, "A robust natural-frame-based interfacing scheme for grid-connected distributed generation inverters," *IEEE Trans. Energy Convers.*, vol. 26, no. 3, pp. 728–736, Sept. 2011.

[29] Y. A.-R. I. Mohamed, E. F. El-Saadany, and M. M. A. Salama, "Adaptive grid-voltage sensorless control scheme for inverter-based distributed generation," *IEEE Trans. Energy Convers.*, vol. 24, no. 3, pp. 683–694, Sept. 2009.

[30] A. Bechouche, H. Sediki, D. Ould Abdeslam, and S. Haddad, "A novel method for identifying parameters of induction motors at standstill using ADALINE," *IEEE Trans. Energy Convers.*, vol. 27, no. 1, pp. 105–116, Mar. 2012.

[31] A. Bechouche, D. Ould Abdeslam, and H. Seddiki, "AC voltage sensorless control of three-phase PWM rectifiers," *in Proc. Int. Renew. Sustain. Energy Conf. (IRSEC)*, Dec. 2015, pp. 1–6.

[32] M. Cirrincione, M. Pucci, and G. Vitale, "A single-phase DG generation unit with shunt active power filter capability by adaptive neural filtering," *IEEE Trans. Ind. Electron.*, vol. 55, no 5, p. 2093–2110, May 2008.

[33] K. J. Astrom and B. Wittenmark, *Adaptive Control*, New York: Addison-Wesley, 1995.

[34] B.Widrow and E.Walace, *Adaptive Inverse Control—A Signal Processing Approach*. Piscataway, NJ: IEEE Press, 2008.

[35] D.-C. Lee and D.-S. Lim, "AC voltage and current sensorless control of three-phase PWM rectifiers," *IEEE Trans. Power Electron.*, vol. 17, no. 6, pp. 883–890, Nov. 2002.

[36] J.-J. Jung, E. Jung, J.-I. Ha, and S.-K. Sul, "Initial voltage angle detection method of a PWM converter without any grid voltage measurement using conduction state of diodes for smooth starting," in Proc. *7th Int. Power Electron. Motion Control Conf. (IPEMC)*, Harbin, China, June 2012, pp. 730–734.

[37] G. D. Marques, "A simple and accurate system simulation of three-phase diode rectifiers," *in Proc. 24th IEEE Annu. Conf. Ind. Electron. Soc., IECON '98*, vol. 1, no. 31, Aug. 31–Sept. 4, 1998, pp. 416–421.

[38] P. Rodriguez, A. Luna, R. S. Munoz-Aguilar, I. Etxeberria-Otadui, R. Teodorescu, and F. Blaabjerg, "A stationary reference frame grid synchronization system for three-phase grid-connected power converters under adverse grid conditions," *IEEE Trans. Power Electron.*, vol. 27, no 1, pp. 99-112, Jan. 2012.

Adel Rahoui was born in Tizi-Ouzou, Algeria, on May 03, 1990. He received the B.Sc. and M.Sc. degrees in electrical engineering from M'Hamed Bougara University, Boumerdes, Algeria, in 2011 and 2013, respectively.

He is currently pursuing the Ph.D. degree at the L2CSP laboratory, Mouloud Mammeri University, Tizi-Ouzou. His research interests include the application of modern control methods and artificial intelligence to AC/DC converters.

Ali Bechouche was born in Tizi-Ouzou, Algeria, on December 09, 1982. He received the Engineer, the Magister, and the Ph.D. degrees in electrical engineering from the Mouloud Mammeri University of Tizi-Ouzou, Tizi-Ouzou, Algeria, in 2007, 2009, and 2013, respectively. He received the Habilitation in electrical engineering from the Mouloud Mammeri University of Tizi-Ouzou, in 2016.

He is currently an Associate Professor in the Department of Electrical Engineering, Mouloud Mammeri University of Tizi-Ouzou. His research interests include electrical drives and advanced control techniques applied to power electronics, photovoltaic systems and wind power generators.

Hamid Seddiki was born in Tizi-Ouzou, Algeria on March 21, 1966. He received Engineer, Magister, and Ph.D. degrees in electrical engineering from the Mouloud Mammeri University of Tizi-Ouzou, Tizi-Ouzou, Algeria in 1991, 2000, and 2010, respectively. He received the Habilitation in electrical engineering from the Mouloud Mammeri University of Tizi-Ouzou in 2012.

Since 1993, he has been with the Mouloud Mammeri University of Tizi-Ouzou, where he is currently an Associate Professor. His main interests include power electronics and electrical drives.

Djaffar Ould Abdeslam (M'08–SM'15) was born in Tizi-Ouzou, Algeria, on April 20, 1976. He received the M.Sc. degree in electrical engineering from the University of Franche-Comté, Besançon, France, in 2002, the Ph.D. degree from the University of Haute-Alsace, Mulhouse, France, in 2005.

From 2007, he is an Associate Professor at the University of Haute-Alsace. He received the Habilitation in Electrical Engineering from the University of Haute-Alsace in 2014. His research interest includes Artificial Neural Networks applied to Power Systems, Signal Processing for Power Quality Improvement, Smart Metering, Smart Building and Smart Grids.

.